

1 Compositional flexibility in irreducible antifluorite electrolytes for 2 next-generation battery anodes

3 Victor Landgraf, Mengfu Tu, Zhu Cheng, Alexandros Vasileiadis, Marnix Wagemaker*, Theodosios
4 Famprakis*

5 Faculty of Applied Sciences, Delft University of Technology, 2629 JB Delft, The Netherlands

6 * t.famprakis@tudelft.nl; m.wagemaker@tudelft.nl

7 Abstract

8 Solid-state batteries currently receive ample attention due to their potential to outperform lithium-ion
9 batteries in terms of energy density when featuring next-generation anodes such as lithium metal or
10 silicon. One key remaining challenge is identifying solid electrolytes that combine high ionic conductivity
11 with stability in contact with the highly reducing potentials of next-generation anodes. *Fully reduced*
12 electrolytes, based on irreducible anions, offer a promising solution by avoiding electrolyte decomposition
13 altogether. In this study, we demonstrate the compositional flexibility of the disordered antifluorite
14 framework accessible by mechanochemical synthesis and leverage it to discover irreducible electrolytes
15 with high ionic conductivities. We show that the recently investigated $\text{Li}_9\text{N}_2\text{Cl}_3$ and Li_5NCl_2 phases are part
16 of the same solid solution of Li-deficient *antifluorite* phases existing on the $\text{LiCl}-\text{Li}_3\text{N}$ tie line with a general
17 chemical formula of $\text{Li}_{1+2x}\text{Cl}_{1-x}\text{N}_x$ ($0.33 < x < 0.5$). Using density functional theory calculations, we identify the
18 origin of the 5-order-of-magnitude conductivity increase of the $\text{Li}_{1+2x}\text{Cl}_{1-x}\text{N}_x$ phases compared to the
19 structurally related *rock-salt* LiCl phase. Finally, we demonstrate that S_{Cl} - and Br_{Cl} -substituted analogues
20 of the $\text{Li}_{1+2x}\text{Cl}_{1-x}\text{N}_x$ phases may be synthesized, enabling significant conductivity improvements by a factor
21 of 10, reaching 0.2 mS cm^{-1} for $\text{Li}_{2.31}\text{S}_{0.41}\text{Br}_{0.14}\text{N}_{0.45}$. This investigation demonstrates for the first time that
22 irreducible antifluorite-like phases are compositionally highly modifiable; this finding lays the ground for
23 discovery of new compositions of irreducible antifluorite-like phases with even further increased
24 conductivities, which could help eliminate solid-electrolyte decomposition and decomposition-induced Li
25 losses on the anode side in high-performance next-generation batteries.

26 Introduction

27 Solid-state batteries have the potential to supersede conventional Li-ion batteries in terms of energy
28 density and safety.^{1,2} Three main advantages of solid electrolytes are as follows. (1) The solid nature of

solid electrolytes potentially enables bipolar stacking of individual cells, increasing the overall pack energy density. (2) Solid electrolytes are typically less flammable than liquid equivalents and thus safer. (3) Solid electrolytes are potentially better compatible with high-energy anodes such as silicon or metallic lithium.^{1,2} An initial challenge has been to develop solid electrolytes with sufficiently high ionic conductivities to compete with liquid electrolytes. In recent years , multiple derivatives of the argyrodite and Li₁₀GeP₂S₁₂ solid electrolytes have been developed with Li-ion conductivities beyond 10 mS cm⁻¹, thus exceeding the conductivities of their liquid equivalents.³⁻⁶ Nevertheless, the main issue with all known high-conducting (>1 mS cm⁻¹) solid electrolytes is that they are not (electro)-chemically stable at the high potentials of typical Li-ion battery cathodes nor at low potentials of desirable high-capacity anodes such as Si or Li metal. The electrochemical instability of solid electrolytes with electrodes inevitably leads to electrolyte decomposition at the electrolyte-electrode interfaces.^{1,7} Electrolyte decomposition at the electrode interfaces causes Li loss, formation of resistive interphases and contact loss between solid-electrolyte- and electrode particles, which are all directly linked to battery degradation and failure.^{8,9}

This study aims to design solid electrolytes that are highly conducting and thermodynamically stable against the low potentials of desirable high-capacity anodes such as lithium metal and silicon. Such electrolytes would eliminate (electro)chemical degradation on the anode side and thus eliminate complications associated with electrolyte degradation. With regards to thermodynamic stability at low potentials, *fully reduced* phases become immediately pertinent; i.e. phases in which the only cation present is Li and in which all anions are in their lowest permitted formal oxidation state and thus irreducible.^{10,11} Commonly known examples of such irreducible phases are the lithium binaries LiCl, LiBr, Li₂S, LiI, LiF, Li₃N and Li₃P. While these phases all feature thermodynamic stability at the low potentials (<0 V vs. Li⁺/Li), they are fraught with low ionic conductivities (<10⁻⁶ mS cm⁻¹), except for Li₃N, which is reported to have a conductivity of 0.5 mS cm⁻¹.^{10,12} New irreducible phases were recently discovered by exploring the tie lines between the above-listed binaries using mechanochemical synthesis. Examples include the Li_{2+x}S_{1-x}P_x phases reported by Szcuka et al.¹¹ and the Li_{2+x}S_{1-x}N_x phases reported by Landgraf et al.¹³; both systems reaching high conductivities of 0.2 mS cm⁻¹. Additionally, the Li₅NCl₂¹⁰ and Li₉N₂Cl₃¹⁴ phases existing on the Li₃N-LiCl tie line were recently investigated. Li et al. demonstrated excellent stability against Li-metal, stability in dry air and high critical-current density for dendrite formation of 10 mA cm⁻² for the Li₉N₂Cl₃ phase.¹⁴ Additionally, excellent performance of Li₉N₂Cl₃ in full cells was demonstrated where Li₉N₂Cl₃ is used as an anolyte to protect the Li_{2.73}Ho_{1.09}Cl₆ halide electrolyte against a Li metal anode.¹⁴ These results are promising, however an essential drawback remains the low room temperature (RT) conductivity of Li₉N₂Cl₃ which is reported to be 0.04 mS cm⁻¹.¹⁴ Moreover, the mechanistic origin of the

61 increased conductivity of $\text{Li}_9\text{N}_2\text{Cl}_3$ phases compared to the structurally related rocksalt LiCl phase has not
62 been established.

63 The present study develops compositional design strategies to improve the conductivity of $\text{Li}_9\text{N}_2\text{Cl}_3$
64 through the following advances:

65 (1) Synthetically, we demonstrate that the antifluorite framework is compositionally flexible; Li-
66 deficient and Li-excess antifluorite phases can be mechanochemically stabilized. We find that the
67 previously reported Li_5NCl_2 and $\text{Li}_9\text{N}_2\text{Cl}_3$ phases (refs. 15,16) are both members of the same solid
68 solution of Li-deficient antifluorite phases on the $\text{Li}_3\text{N}-\text{LiCl}$ tie line with the general chemical
69 formula of $\text{Li}_{1+2x}\text{Cl}_{1-x}\text{N}_x$ with $0.33 < x < 0.5$. Additionally, we show that $\text{Li}_{1+2x}\text{Cl}_{1-x}\text{N}_x$ phases are
70 compositionally highly modifiable; we synthesize S_{Cl} - and Br_{Cl} -substituted analogues boosting the
71 ionic conductivities of $\text{Li}_{1+2x}\text{Cl}_{1-x}\text{N}_x$ phases by an order of magnitude enabling conductivity
72 enhancements up to 0.2 mS cm^{-1} for $\text{Li}_{2.31}\text{S}_{0.41}\text{Br}_{0.14}\text{N}_{0.45}$.

73 (2) Computationally, we explain how introducing nitrogen into the LiCl anionic-framework brings
74 tetrahedral and octahedral lithium sites closer in energy so that vacant sites become energetically
75 accessible for diffusion. Our analysis of diffusion bottlenecks resolving the effect of the local anion
76 coordination shows that nitrogen widens diffusion bottlenecks further facilitating Li diffusion.

77 (3) Finally, we find through both experiments and computations that the oxidation limit of the
78 irreducible antifluorite-like phases is compositionally tunable and generally higher compared to
79 Li_3N which may be a critical advantage to stabilize next-generation anodes.

80 Results and Discussion

81 Our starting point for this work is our previous work on fully reduced electrolytes, showing the
82 conductivity of Li_2S could be highly improved by dissolving Li_3N into the antifluorite Li_2S phase.¹³ Dissolving
83 Li_3N in Li_2S results in a series of phases where N and S share sites (Figure S1). A solid solution exists with
84 the general chemical formula $\text{Li}_{2+x}\text{S}_{1-x}\text{N}_x$ ($0 < x < \sim 0.5$), exhibiting an anion-disordered Li-rich antifluorite
85 crystal structure (Figure S1) and showing much higher conductivity ($> 0.2 \text{ mS cm}^{-1}$ for $x=0.5$) than the Li_2S
86 host phase ($10^{-6} \text{ mS cm}^{-1}$) (see Figure S1).¹³ This motivated our investigation of whether a similar solid
87 solution may be found between Li_3N and LiCl (schematically illustrated in Figure 1a), and examine their
88 functional solid-electrolyte properties. To answer this question, Li_3N and LiCl were mixed in different
89 ratios, followed by a high-energy mechanochemical treatment (*ball milling*).

90 A solid solution of Li-deficient antifluorite phases on the $\text{Li}_3\text{N}-\text{LiCl}$ tie line

91 Figure 1 presents the results of the mechanochemical treatment of x Li₃N + (1-x) LiCl samples and their
92 resulting structure and ionic conductivities. Figure 1a presents schematically the crystal structures of the
93 parent LiCl rocksalt phase and the target antifluorite phases, confirmed by the powder x-ray diffraction
94 experiments shown in Figure 1b. Attempting to dissolve small quantities of Li₃N into LiCl did not result in
95 a pure phase but a mixture of two cubic phases: LiCl and Li₅NCl₂. The stoichiometric formula of the latter
96 may alternatively be written as Li_{1.66}N_{0.33}Cl_{0.66} (i.e. Li_{1+2x}Cl_{1-x}N_x with x=0.33), and has been previously
97 reported as a stable phase prepared by conventional solid-state synthesis.^{10,15} Only when the
98 Li_{1.66}N_{0.33}Cl_{0.66} stoichiometry is reached, having a 2:1 LiCl/Li₃N ratio, a pure Li_{1.66}N_{0.33}Cl_{0.66} phase is observed
99 (i.e. the LiCl phase is not observed in the X-ray diffraction pattern). The mixtures with a higher nitrogen
100 composition than the Li_{1.66}N_{0.33}Cl_{0.66} phase (Li_{1+2x}Cl_{1-x}N_x with 0.33< x <0.5) show the same cubic $Fm\bar{3}m$
101 diffraction pattern as the x=0.33 phase but with an increasing shift towards larger scattering vector Q
102 indicating a decreasing lattice parameter with increasing nitrogen content. When exceeding an overall
103 stoichiometry of Li₂N_{0.5}Cl_{0.5} (i.e. x=0.5) a second phase identified as β -Li₃N is observed in the diffraction
104 pattern while the lattice parameter of the first phase remains constant. As expected based on the smaller
105 ionic radius of N³⁻ compared to Cl⁻ (1.46 vs 1.81 Å),¹⁷ the lattice parameter of the Li_{1+2x}Cl_{1-x}N_x phases
106 decreases with increasing nitrogen content, where the linear shift is in accordance with Vegard's law
107 (Figure 1c). A solid-solution region of cubic Li_{1+2x}Cl_{1-x}N_x phases is thus observed on the x-LiCl-(1-x)Li₃N tie line for compositions between 0.33< x <0.5, i.e. between the end members
108 Li_{1.66}N_{0.33}Cl_{0.66} and Li₂N_{0.5}Cl_{0.5}.
109

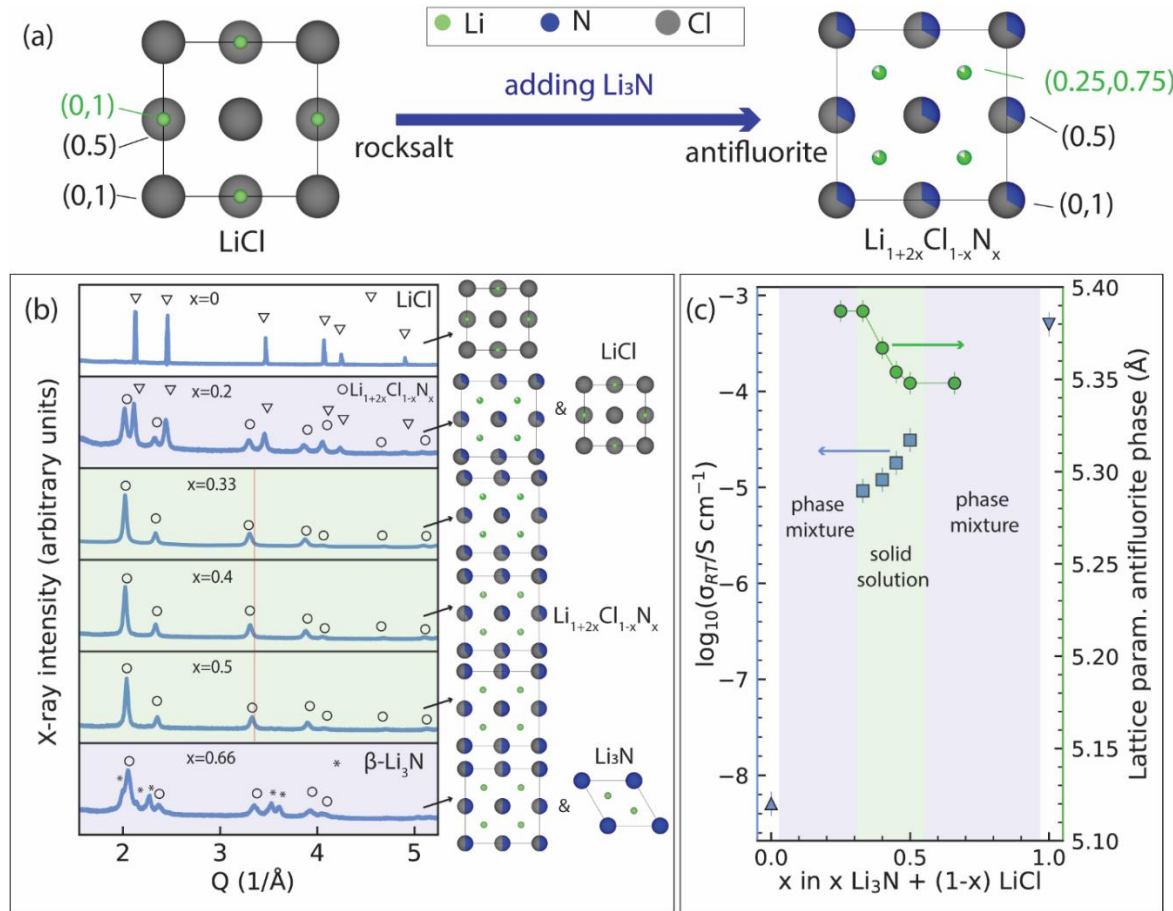


Figure 1. Discovery of a new solid solution on the $\text{Li}_3\text{N}-\text{LiCl}$ tie line. (a) View along the [001] of the unit cell of rock-salt LiCl and Li-deficient antifluorite $\text{Li}_{1+2x}\text{Cl}_{1-x}\text{N}_x$ phases (exact example of $x=0.33$ shown). (b) X-ray diffraction pattern of the products of mechanochemically treating $x \text{ Li}_3\text{N} + (1-x) \text{ LiCl}$ mixtures. In the range ($x=0.33$ to $x=0.5$) phase-pure Li-deficient antifluorite structures are obtained. Phases existing at each overall composition are shown next to the diffraction patterns. Red line is guide to the eye. (c) Overall ionic conductivity at 22 °C determined experimentally via impedance spectroscopy and the lattice parameter of the antifluorite-like phase for different mixtures of $x \text{ Li}_3\text{N} + (1-x) \text{ LiCl}$. Conductivity of (structurally distinct) Li_3N and LiCl are also shown for reference. Green and purple shading in (b) and (c) indicate solid-solution- and two-phase- regions, respectively.

110 Rietveld refinements of the x-ray diffractograms (SI Figure S2 and Tables S1-4) show that the crystal
 111 structure of the $\text{Li}_{1+2x}\text{Cl}_{1-x}\text{N}_x$ ($x < 0.33 < 0.5$) phases consist in a face-centered-cubic arrangement of the
 112 anions where N^{3-} and Cl^- share the same site. At the nitrogen-poor boundary of the solid solution (i.e.

113 $\text{Li}_{1.66}\text{N}_{0.33}\text{Cl}_{0.66}$) the tetrahedral interstitials are partially occupied by Li ions (83%).* With increasing N
114 content the Li content increases to balance the charge, and the tetrahedral sites become increasingly
115 populated until reaching the N-rich solid-solution boundary (i.e. $\text{Li}_2\text{N}_{0.5}\text{Cl}_{0.5}$). Consequently, where the
116 $\text{Li}_2\text{N}_{0.5}\text{Cl}_{0.5}$ phase can be described as a (stoichiometric) antifluorite phase (with fully occupied tetrahedral
117 sites), the solid-solution members with ($x < 0.5$) may be described as Li-deficient antifluorite phases (having
118 only partially occupied tetrahedral sites). Further lithium insertion ($x > 0.5$) seems to destabilize the
119 antifluorite, leading to decomposition into a mixture of $\text{Li}_2\text{Cl}_{0.5}\text{N}_{0.5}$ and Li_3N (Figure 1b). This is in contrast
120 to the lithium-rich antifluorites $\text{Li}_{2+x}\text{S}_{1-x}\text{N}_x$ which exhibit partial occupation of their octahedral sites in
121 addition to full occupation of their tetrahedral sites (*vide infra*). The structural shift that occurs when going
122 from rock-salt LiCl to Li-deficient antifluorite $\text{Li}_{1.66}\text{N}_{0.33}\text{Cl}_{0.66}$ entails a significant increase of the cubic lattice
123 parameter from 5.17 Å to 5.39 Å (Figure 1b), which is likely related to the rearrangement of lithium from
124 the octahedral sites (in the former) to tetrahedral sites (in the latter).

125 Figure 1c also shows the ambient-temperature ionic conductivity of the mechanochemically prepared
126 samples as quantified by impedance spectroscopy experiments on pelletized samples which could be
127 invariably fitted by a single bulk-diffusion process (SI Figure S3). The rock-salt LiCl phase has a conductivity
128 of the order of $10^{-7} \text{ mS cm}^{-1}$ (Figure S4). The conductivity of Li-deficient antifluorite $\text{Li}_{1.66}\text{N}_{0.33}\text{Cl}_{0.66}$ is
129 significantly higher reaching 0.01 mS cm^{-1} , and introducing more nitrogen into the solid solution further
130 increases the conductivity up to 0.03 mS cm^{-1} for $\text{Li}_2\text{N}_{0.5}\text{Cl}_{0.5}$ as shown in Figure 1c.

131 We have thus discovered a new solid solution on the $\text{LiCl}-\text{Li}_3\text{N}$ tie line with the general formula $\text{Li}_{1+2x}\text{Cl}_{1-x}\text{N}_x$
132 ($x < 0.33 < 0.5$) accessible by mechanochemistry (in contrast to conventional solid state synthesis previously
133 explored in refs.^{10,15}). These phases crystallize in an anion disordered Li-deficient antifluorite-like crystal
134 structure and their conductivity is orders of magnitude higher than the conductivity of rock-salt LiCl . In
135 the next section, we will analyze the mechanistic origin of this 5-order-of-magnitude boost in ionic
136 conductivity.

137 **Rock-salt LiCl vs. Li-deficient antifluorite $\text{Li}_{1+2x}\text{Cl}_{1-x}\text{N}_x$ – origin of the improved conductivity**

138 Fast Li diffusion relies on two prerequisites: (1) Li sites connected by low Li-hop activation energies into a
139 percolating network and (2) a sufficient fraction of vacancies among these Li sites. Vacant Li-sites may be
140 introduced by defects (e.g. Frenkel defect pairs) and/or may be synthetically introduced via compositional

* A small fraction of the Li ions ≤5% may potentially occupy the octahedral sites as detailed in Supplementary Note 1.

141 tuning. To investigate Li diffusion in (defect-free) rock-salt LiCl and Li-deficient antifluorite $\text{Li}_{1+2x}\text{Cl}_{1-x}\text{N}_x$
142 phases we performed *ab initio* molecular dynamics (AIMD) simulations of (2x2x2) LiCl supercells. As done
143 in previous studies, we dissected our AIMD simulations into individual jump events.^{10,18–21} From the
144 frequency of jumps between two sites A and B ($v_{A \rightarrow B}$), we calculate jump-activation energies (jump-E_a) by
145 using equation (1) and assuming a prefactor frequency (v_0) of 10^{13} Hz: ^{†*}

146
$$\text{jump } E_{a,A \rightarrow B} = -k_b T \ln \left(\frac{v_{A \rightarrow B}}{v_0} \right) \quad (1)$$

147 where k_b is the Boltzmann constant, T the temperature in K, $v_{A \rightarrow B}$ the observed frequency of jumps
148 between sites A and B and jump-E_{a, A → B} the jump-activation energy of a jump event from site A to site B.
149 Details on this methodology may be found in refs.^{18,22} We use these jump-activation energies as a proxy
150 for the local energy barriers. From the difference between the activation energies of the forward and
151 backward jump, the energy difference between two crystallographic positions may be approximated as
152 follows (and illustrated in Figure S5):

153
$$\Delta E_{\text{site}}(A, B) = | \text{jump } E_{a,A \rightarrow B} - \text{jump } E_{a,B \rightarrow A} | \quad (2)$$

154 $|\Delta E_{\text{site}}(\text{tet, oct})|$ may be approximated from equation 2 as the average of $\Delta E_{\text{site}}(A, B)$ for all sites where A
155 and B are tetrahedral and octahedral sites respectively.

156 Figure 2 presents the result of our analysis of molecular dynamics of rock-salt LiCl and Li-deficient
157 antifluorite $\text{Li}_{1+2x}\text{Cl}_{1-x}\text{N}_x$ phases

[†] Assuming $v_0 = 10^{13} \text{ s}^{-1}$ is commonly adopted in the solid electrolyte field.^{19,44,45} Additionally we justify this choice by calculating the average vibration frequency around the equilibrium Li-sites in our AIMD simulations and find it to be $1.0 \pm 0.2 \cdot 10^{13} \text{ Hz}$ for 5 different $\text{Li}_{1+2x}\text{Cl}_{1-x}\text{N}_x$ supercells (Table S5).

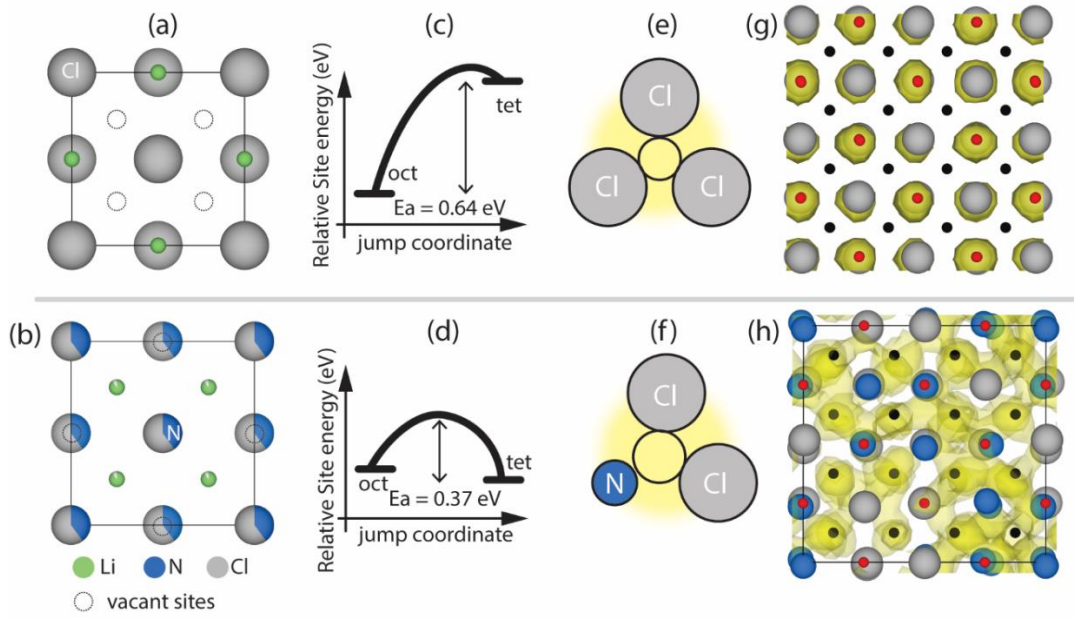


Figure 2. Comparison Lithium diffusion in LiCl and $\text{Li}_{1+2x}\text{Cl}_{1-x}\text{N}_x$ phases via ab initio molecular dynamics simulations. (a) and (b) View along the [001] of the unit cell of rock-salt LiCl and Li-deficient antifluorite $\text{Li}_{1+2x}\text{Cl}_{1-x}\text{N}_x$ phases. (c) and (d) Schematic illustration of the energy difference and average jump-activation energy between tetrahedral and octahedral sites in rock-salt LiCl and Li-deficient antifluorite $\text{Li}_{1+2x}\text{Cl}_{1-x}\text{N}_x$ phases. (e) and (f) Schematics of the triangular bottlenecks for oct-tet jumps. (g) and (h) LiCl and $\text{Li}_{1.8}\text{Cl}_{0.6}\text{N}_{0.4}$ supercell with the Li density of a 100 ps AIMD simulation at 1000 K. The Li density cutoff is set to 3% of the maximum value.

158 In LiCl, the octahedral interstitials are preferably occupied over the tetrahedral ones (Figure 2a), indicating
 159 that the former are more stable than the latter. All tetrahedral interstitials in LiCl are vacant thus, in
 160 principle, LiCl features a high concentration of vacant interstitials enabling potential diffusion pathways
 161 via an octahedral-tetrahedral-octahedral jump sequence $|\Delta E_{\text{site}}(\text{tet}, \text{oct})|$ is 0.61 ± 0.02 eV in the case of
 162 LiCl indicating that tetrahedral sites are on average significantly destabilized by ca. 0.6 eV versus
 163 octahedral sites. The jump-activation energy for the tet-oct jumps in LiCl is low (ca. 0.03 eV) suggesting
 164 that the tetrahedral site is highly metastable and should arguably more generally be referred to as
 165 ‘position’ than ‘site’ as further detailed in Supplementary Note 2. For the remaining discussion of this work
 166 however this distinction will not be made and the tetrahedral positions in LiCl will also be referred to as
 167 sites. One potential reason for the high metastability of tetrahedral Li sites may be the small void space

168 at the tetrahedral site enabling occupation of an ion with a max radius of 0.38 Å (see Supplementary Note
169 3) which is smaller than the Li-ion radius (0.59 Å).¹⁷ Additionally, oct-tet transitions are sterically hindered
170 in LiCl due to a highly constrained bottleneck with a diameter of 0.8 Å, which requires energetically
171 unfavorably close Li-Cl ion distances and/or lattice distortion to accommodate the passing of Li ions
172 (Figure 2e). To summarize, in rock-salt LiCl, Li is confined to the octahedral sites and low-activation-energy
173 jumps to vacant sites are not available, rationalizing the absence of diffusion during simulations (localized
174 density in Figure 2g) and the low RT ion conductivity of LiCl.[‡]

175 We now turn our attention to Li-diffusion in the $\text{Li}_{1.66}\text{N}_{0.33}\text{Cl}_{0.66}$ phase. We performed AIMD simulations on
176 seven different disordered $\text{Li}_{1+2x}\text{Cl}_{1-x}\text{N}_x$ (2x2x2) supercells (including $\text{Li}_{1.66}\text{N}_{0.33}\text{Cl}_{0.66}$) to investigate the ion
177 jumps and their jump activation energies present in these phases. Shared site occupations and partial
178 occupancies in $\text{Li}_{1+2x}\text{Cl}_{1-x}\text{N}_x$ phases were treated by random decoration of the Wyckoff 4a (0,0,0) position
179 with nitrogen and chlorine and the 8c (0.25,0.25,0.25). Li-positions were randomly decorated with Li and
180 vacancies in order to reach the targeted stoichiometry (See methodology for full computational details).
181 In contrast to LiCl, in the Li-deficient antifluorite $\text{Li}_{1.66}\text{N}_{0.33}\text{Cl}_{0.66}$ structure the tetrahedral Li sites are
182 occupied, indicating that they are stabilized with respect to the octahedral sites. $\text{Li}_{1.66}\text{N}_{0.33}\text{Cl}_{0.66}$ features
183 two types of intrinsic vacancies. (1) the tetrahedral sites are partially occupied and (2) the octahedral
184 interstitials are essentially vacant (Figure 2b).[§] Compared to LiCl the difference in site energy between
185 octahedral and tetrahedral is much smaller, with $|\Delta E_{\text{site}}(\text{tet-oct})| = 0.07 \pm 0.01$ eV as compared to
186 $|\Delta E_{\text{site}}(\text{tet-oct})| = 0.61 \pm 0.02$ eV in LiCl (Figure 2c and d). This flat(ter) energy landscape enables low-
187 activation-energy oct-tet jumps and increased bulk diffusion reflected in the much more diffuse Li-density
188 compared to the LiCl case (Figure 2h) and higher experimentally-measured conductivities of $\text{Li}_{1.66}\text{N}_{0.33}\text{Cl}_{0.66}$
189 (Figure 1c).

190 Figure 3 presents our analysis of ion hopping in disordered $\text{Li}_{1+2x}\text{Cl}_{1-x}\text{N}_x$ as a function of local environment
191 and jump geometry.

[‡] Due to the high activation energy required for oct-tet jumps in LiCl and the high metastability of tet sites/positions diffusion in LiCl is likely mediated by Schottky defects just as in NaCl. Accordingly, the charge carrier concentration in LiCl at room temperature is extremely low ($\sim 1 \times 10^{-9} \text{ c}_{\text{Li}}$ where c_{Li} is the Li concentration in LiCl) as the formation energy for Schottky defects is typically ~ 1 eV. This low charge carrier concentration additionally contributes to the low ionic conductivity in LiCl.

[§] Potentially a small fraction of Li ions $\leq 5\%$ on average may occupy the octahedral sites in which case the octahedral sites as detailed in Supplementary Note 1.

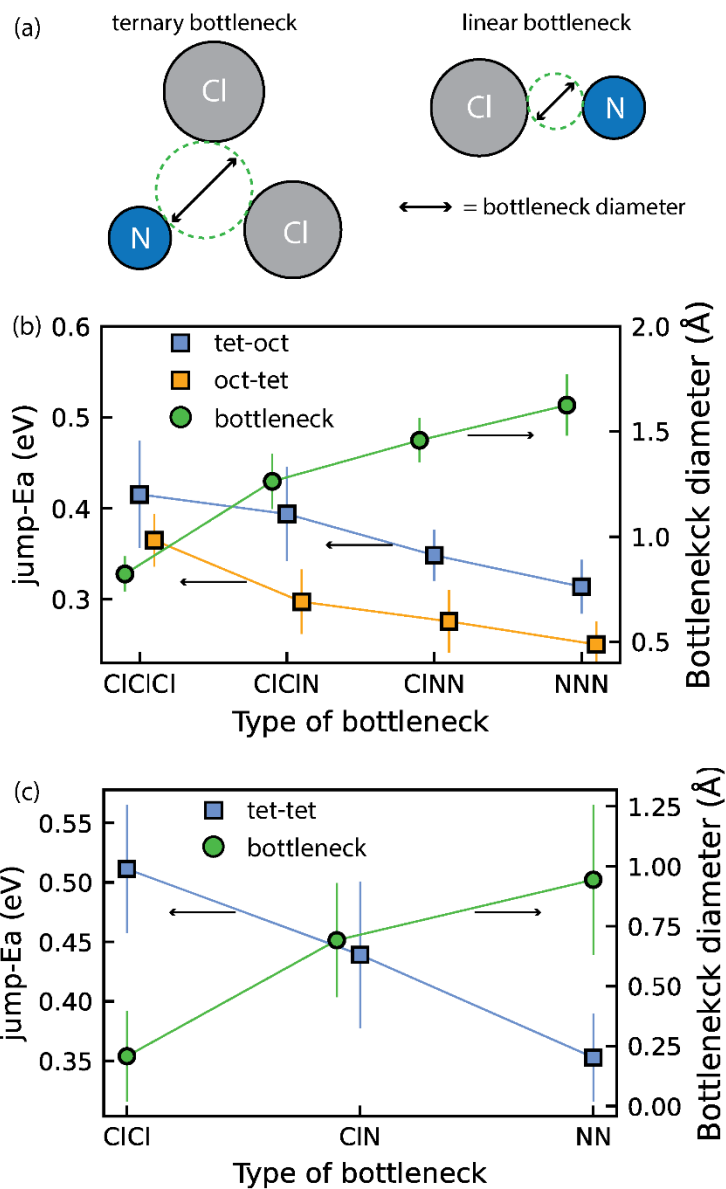


Figure 3. Jump activation energies and bottleneck sizes for ion hops through specific bottlenecks. (a) and (b) Schematic of triangular and linear bottlenecks connecting oct-tet and tet-tet site pairs, respectively. (c) Average activation energy of tet-oct and oct-tet jumps for different bottleneck compositions along with the bottleneck size. Error bars are the standard deviation of the distribution of observed bottleneck sizes and activation energies. (d) Same as (c) for tet-tet jumps.

192 From our AIMD simulations we observe that diffusion occurs via Li jumps between oct and tet sites
 193 through triangular bottlenecks consisting of three anions (Figure 3a) as well as between tet sites through
 194 linear bottlenecks consisting of two anions (Figure 3b). Li diffusion through triangular and linear

195 bottlenecks is facilitated by the presence of N in the anionic lattice. Because N^{3-} (1.46 Å) anions are
196 considerably smaller than Cl^- (1.81 Å) anions, the bottleneck becomes larger, enabling Li diffusion. To
197 quantify this further, we calculated the bottleneck diameters for 5 $\text{Li}_{1.66}\text{N}_{0.33}\text{Cl}_{0.66}$ DFT relaxed (2x2x2)
198 supercells (featuring >500 bottlenecks) to account for local distortions that may not be evident in the
199 average crystallographic unit cell. The bottleneck diameters for different bottlenecks as well as the
200 average jump-E_a for jumps through the respective bottlenecks are shown in Figure 3. Comparing the
201 bottleneck diameter to the diameter of Li-ions (1.18 Å) is a good proxy for the constraints on Li diffusion;
202 bottlenecks with significantly smaller diameters than 1.18 Å will constrain Li diffusion more than
203 bottlenecks with diameters > 1.18 Å. Figure 3a and 3b for instance shows that triangular bottlenecks
204 consisting of three chlorides are considerably smaller (~0.8 Å) than bottlenecks containing one or more
205 nitrogen (>1.25 Å). Figure 3c and 3d show that jumps through nitrogen-containing bottlenecks for oct-tet
206 and tet-tet jumps have lower activation energies indicating easier diffusion through N containing
207 bottlenecks. Consequently, increasing the nitrogen content in the $\text{Li}_{1+2x}\text{Cl}_{1-x}\text{N}_x$ phase, results in more
208 nitrogen-rich, low-activation-energy bottlenecks, explaining the increase in conductivity upon increasing
209 the nitrogen content in the $\text{Li}_{1+2x}\text{Cl}_{1-x}\text{N}_x$ solid solution shown in Figure 1c.

210 In conclusion, it is not possible to continuously dissolve Li_3N into rock-salt LiCl to form Li-excess rock-salt
211 phases as the excess Li ions would occupy tetrahedral sites which are sterically too constrained to
212 accommodate Li ions. However, once a critical amount of Li_3N ($x \geq 0.33$) is mixed with LiCl sufficient Li ions
213 are available to stabilize (Li-deficient) antifluorite phases where Li ions occupy tetrahedral sites. The
214 occupation of tetrahedral sites indicates that the tetrahedral sites are more stable than octahedral sites
215 in Li-deficient antifluorite phases. The vacant octahedral sites and the occupied tetrahedral sites are
216 energetically in close proximity ($|\Delta E_{\text{site}}(\text{tet-oct})| \sim 0.07$ eV) and oct-tet (and tet-tet) transitions are
217 facilitated by the presence of N^{3-} anions in the anionic lattice as the smaller ionic radius of N^{3-} compared
218 to Cl^- increases the bottleneck size (Figure 2f and 3c). Consequently, the vacant octahedral sites which are
219 innate to Li-deficient antifluorite phases are thermodynamically and kinetically accessible so that tet-oct
220 jumps may be achieved with jump-E_a values of 0.37 ± 0.01 eV on average. In contrast, in LiCl the vacant
221 tetrahedral sites are at much larger energies than the occupied octahedral sites ($|\Delta E_{\text{site}}(\text{tet-oct})| \sim 0.6$ eV).
222 Additionally, the oct-tet transitions are sterically hindered by small bottlenecks consisting of 3 Cl^- ions so
223 that an oct-tet transition has a jump-E_a value of 0.64 ± 0.01 eV on average. Consequently, the vacant
224 tetrahedral sites which are innate to rock-salt LiCl phases are thermodynamically and kinetically
225 inaccessible explaining the absence of diffusion in simulations and the experimentally obtained low ionic
226 conductivity.

227 **Comparison between Li-rich antifluorite $\text{Li}_{2+x}\text{S}_{1-x}\text{N}_x$ and Li-deficient antifluorite $\text{Li}_{1+2x}\text{Cl}_{1-x}\text{N}_x$**

228 The presently discovered $\text{Li}_{1+2x}\text{Cl}_{1-x}\text{N}_x$ ($0.33 < x < 0.5$) solid-solution phases are a structural analog of the
229 $\text{Li}_{2+x}\text{S}_{1-x}\text{N}_x$ ($0 < x < 0.5$) system previously discovered.¹³ Comparing the $\text{Li}_{1+2x}\text{Cl}_{1-x}\text{N}_x$ and $\text{Li}_{2+x}\text{S}_{1-x}\text{N}_x$ phases in
230 the ($0.33 < x < 0.5$) range, where both exist as solid solutions, is insightful in understanding the relationship
231 between structure and Li-ion conductivity. For this we consider three phases of each solid solution, $x=0.33$,
232 $x=0.4$ and $x=0.45$, —representing the lower, center and upper limit of the $0.33 < x < 0.5$ range, respectively—
233 and compare their ionic conductivity metrics as quantified by variable-temperature impedance
234 spectroscopy. Figure 4 presents resulting dependence of the ambient-temperature conductivity,
235 activation energy and conductivity prefactor as a function of composition in $\text{Li}_{1+2x}\text{Cl}_{1-x}\text{N}_x$ and $\text{Li}_{2+x}\text{S}_{1-x}\text{N}_x$.

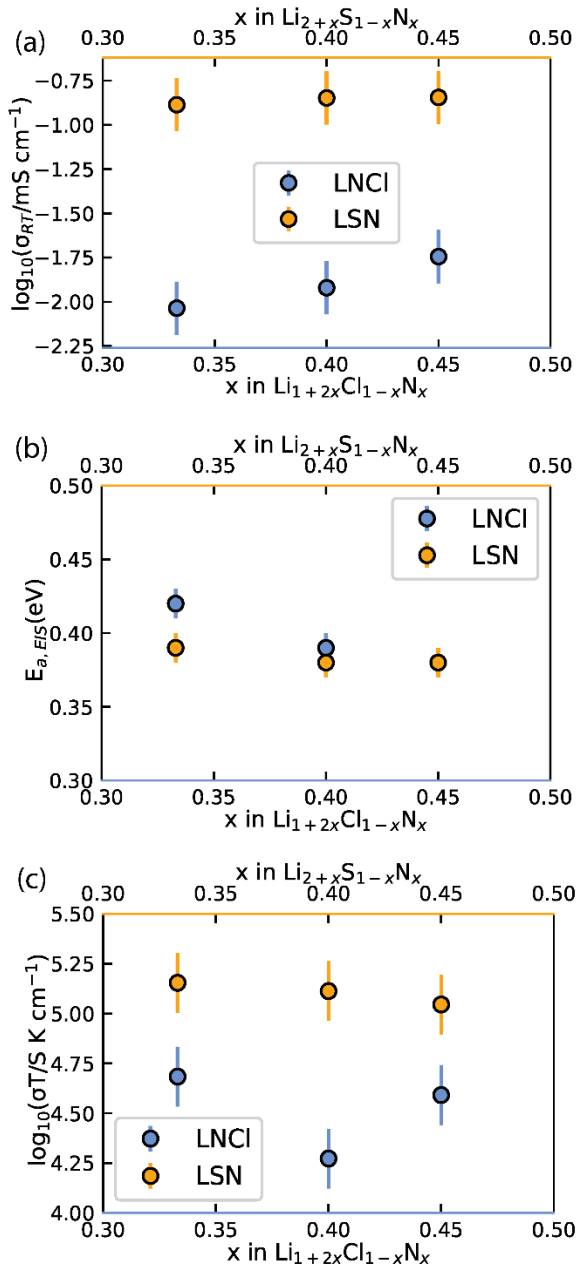


Figure 4. Comparison of the experimentally obtained conductivity, activation energy and Arrhenius prefactor of $\text{Li}_{1+2x}\text{Cl}_{1-x}\text{N}_x$ and $\text{Li}_{2+x}\text{S}_{1-x}\text{N}_x$ phases. (a) Comparison of the conductivity at 22 °C determined experimentally via impedance spectroscopy. (b) Comparison of the Arrhenius plot for the activation energy. (c) Comparison of the Arrhenius prefactor. The Arrhenius fits for (b) are shown in Figure S6.

Data for $\text{Li}_{2+x}\text{S}_{1-x}\text{N}_x$ originally reported in ref. ¹³

236 A notable difference is that the $\text{Li}_{2+x}\text{S}_{1-x}\text{N}_x$ phases are Li-excess antifluorite structures (more than 2 Li per
 237 anion), with partial Li occupancy of the octahedral sites (ref 13) while the $\text{Li}_{1+2x}\text{Cl}_{1-x}\text{N}_x$ phases are Li-

deficient antifluorite phases (less than 2 Li per anion) where the tetrahedral sites are partially occupied by Li (Figures S1-2). Figure 4a shows that the Li-excess $\text{Li}_{2+x}\text{S}_{1-x}\text{N}_x$ phases have much higher ($\sim 10x$) conductivity than the Li-deficient $\text{Li}_{1+2x}\text{Cl}_{1-x}\text{N}_x$ phases, whereas the bulk activation energies, determined by EIS, for the $\text{Li}_{2+x}\text{S}_{1-x}\text{N}_x$ and the $\text{Li}_{1+2x}\text{Cl}_{1-x}\text{N}_x$ phases differ by at most 0.03 eV (Figure 4b) suggesting that the energy thresholds for diffusion in both systems are similar. However, the difference in the Arrhenius prefactors is large, on average a factor of 7 larger for the phases compared to of the $\text{Li}_{1+2x}\text{Cl}_{1-x}\text{N}_x$ phases (Figure 4c). This suggests that the origin of the higher conductivity of $\text{Li}_{2+x}\text{S}_{1-x}\text{N}_x$ phases is largely comprised in the Arrhenius prefactor. The larger charge carrier concentration in $\text{Li}_{2+x}\text{S}_{1-x}\text{N}_x$ (and potentially the inducing of concerted motion though we do not explicitly investigate this here) are likely the origin for the larger Arrhenius prefactor of Li-excess $\text{Li}_{2+x}\text{S}_{1-x}\text{N}_x$ antifluorite phases.

248 **Oxidation limits of Li-rich antifluorite $\text{Li}_{2+x}\text{S}_{1-x}\text{N}_x$ and Li-deficient antifluorite $\text{Li}_{1+2x}\text{Cl}_{1-x}\text{N}_x$ phases**

249 We computationally investigated the metastability of $\text{Li}_{2+x}\text{S}_{1-x}\text{N}_x$ and $\text{Li}_{1+2x}\text{Cl}_{1-x}\text{N}_x$ antifluorite-like phases.
250 For compositions ($x=0.11, 0.17, 0.36, 0.55, 0.72$) we built 10000 random (2x2x2) antifluorite-like $\text{Li}_{2+x}\text{S}_{1-x}\text{N}_x$
251 supercells and calculated their electrostatic energies with the formal oxidation states Li^+ , S^{2-} and N^{3-}
252 assigned to the ions. We took the 30 supercells with the lowest electrostatic energies and relaxed the
253 structures using density functional theory. With the energies obtained, the energy above the hull of these
254 phases was calculated using entries of the materials project database (see also Supplementary Note 4).
255 Figure 5 compares the calculated energies with the experimentally obtained stability limits of $\text{Li}_{2+x}\text{S}_{1-x}\text{N}_x$
256 and $\text{Li}_{1+2x}\text{Cl}_{1-x}\text{N}_x$ as a function of composition.

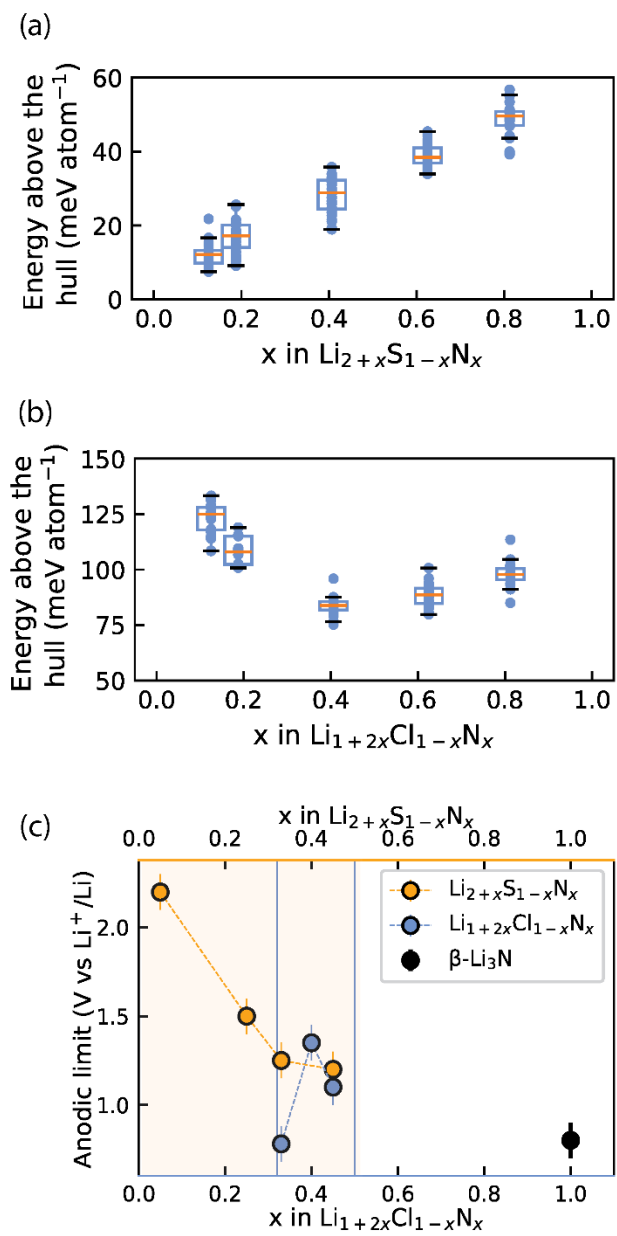


Figure 5. Interplay of phase (meta)stability and anodic limit of irreducible antifluorite phases. (a) and (b) Calculated energy above the hull for 30 $\text{Li}_{2+x}\text{N}_x\text{S}_{1-x}$ and $\text{Li}_{1+2x}\text{Cl}_{1-x}\text{N}_x$ antifluorite supercells at each of several compositions x . At each composition above the distribution of energies above the hull is shown as a box plot where the orange line indicates the arithmetic mean and the box indicates the first standard deviation. (c) Experimental anodic limits obtained from LSV for $\text{Li}_{2+x}\text{S}_{1-x}\text{N}_x$, $\text{Li}_{1+2x}\text{Cl}_{1-x}\text{N}_x$ and $\beta\text{-Li}_3\text{N}$ for reference. Orange shading and blue lines denote the solid-solution range for $\text{Li}_{2+x}\text{S}_{1-x}\text{N}_x$ and $\text{Li}_{1+2x}\text{Cl}_{1-x}\text{N}_x$ respectively. Data for $\text{Li}_{2+x}\text{S}_{1-x}\text{N}_x$ in (c) originally reported in ref.¹³

257 Figure 5a shows the average energy above the hull for the $\text{Li}_{2+x}\text{S}_{1-x}\text{N}_x$ phases and shows that increased
258 nitrogen content and Li stuffing increase metastability (i.e. higher energy above the hull). Note the energy
259 above the hull was calculated for antifluorite-like $\text{Li}_{2+x}\text{S}_{1-x}\text{N}_x$ phases even at nitrogen contents that cannot
260 be stabilized experimentally (i.e. $x>0.55$) to clearly demonstrate the effect of Li_3N dissolution into Li_2S on
261 phase (meta)stability.

262 Turning to the $\text{Li}_{1+2x}\text{Cl}_{1-x}\text{N}_x$ phases, the metastability of $\text{Li}_{1+2x}\text{Cl}_{1-x}\text{N}_x$ phases was calculated in an analogous
263 manner to the $\text{Li}_{2+x}\text{S}_{1-x}\text{N}_x$ phases and is shown in Figure 5b. Note the energy above the hull is calculated for
264 antifluorite-like $\text{Li}_{1+2x}\text{Cl}_{1-x}\text{N}_x$ phases even at nitrogen contents that cannot be stabilized experimentally (i.e.
265 $x<0.33$ and $x>0.5$) to clearly demonstrate the effect of nitrogen content on phase (meta)stability. For
266 $\text{Li}_{1+2x}\text{Cl}_{1-x}\text{N}_x$ phases the metastability is high at low and at high nitrogen content. The metastability of
267 $\text{Li}_{1+2x}\text{Cl}_{1-x}\text{N}_x$ phases is lowest around the center of the $\text{LiCl}-\text{Li}_3\text{N}$ tie line. This non-monotonic trend in the
268 metastability is consistent with the experimentally observed low-N-content and high-N-content
269 boundaries of the $\text{Li}_{1+2x}\text{Cl}_{1-x}\text{N}_x$ ($0.33<x<0.5$) solid solution.

270 Figure 5c presents the oxidative stability limits of the $\text{Li}_{2+x}\text{S}_{1-x}\text{N}_x$ and $\text{Li}_{1+2x}\text{Cl}_{1-x}\text{N}_x$ antifluorite-like phases as
271 determined by linear-sweep voltammetry (SI Figures S7 and S8). The trends in the experimental oxidative
272 limits mirror the trends observed for energy above the hull in Figures 5a and 5b: The increased
273 metastability of N-rich antifluorite-like $\text{Li}_{2+x}\text{S}_{1-x}\text{N}_x$ phases is reflected in the oxidation stability which
274 monotonically decreases the higher the nitrogen content and a non-monotonic trend is observed in the
275 oxidation stability of $\text{Li}_{1+2x}\text{Cl}_{1-x}\text{N}_x$ phases with a maximum for $x=0.4$.

276 **S_{Cl} and Br_{Cl} substitutions on $\text{Li}_{1+2x}\text{Cl}_{1-x}\text{N}_x$ phases to boost conductivity**

277 In this section we investigate the effect of S_{Cl} and Br_{Cl} substitutions in $\text{Li}_{1+2x}\text{Cl}_{1-x}\text{N}_x$ phases. S_{Cl} substitutions
278 in $\text{Li}_{1+2x}\text{Cl}_{1-x}\text{N}_x$ may increase the number of charge carriers and Br_{Cl} substitutions could increase the lattice
279 parameter facilitating Li diffusion. To narrow down this vast compositional space, the effect of the S_{Cl} , Br_{s}
280 and Br_{Cl} substitutions considered at a fixed nitrogen content $x=0.45$. Thus the phase space we set out to
281 investigate can be expressed by the following solid-solution formula: $\text{Li}_{1.9+0.55y}\text{Cl}_{0.55(1-y-z)}\text{S}_{0.55y}\text{Br}_{0.55z}\text{N}_{0.45}$
282 ($0<y,z<1$). We explored the ionic conductivity of this phase space by synthesizing various compositions in
283 the ternary phase diagram and measuring their ionic conductivity using impedance spectroscopy
284 (provided a single antifluorite-like phase was obtained). The results of this investigation are shown in SI
285 Figures S9-S14. Figure 6 presents the ionic conductivity of ternary and quaternary $\text{Li}_{1.9+0.55y}\text{Cl}_{0.55(1-y-$

286 z) $S_{0.55y}Br_{0.55z}N_{0.45}$ antifluorite-like samples synthesized as a function of composition in a quasi-ternary phase
287 diagram.

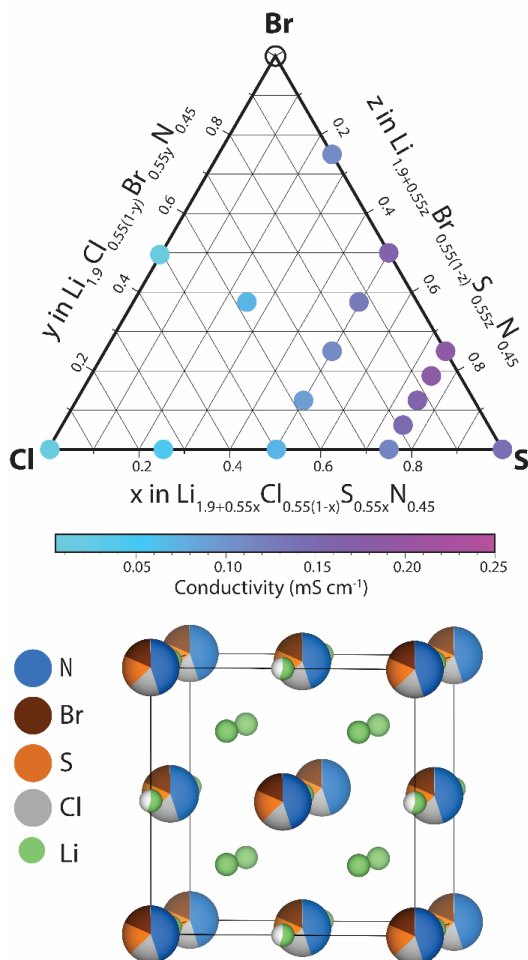


Figure 6. Investigating conductivities in the $Li_{1.9+0.55y}Cl_{0.55(1-y-z)}S_{0.55y}Br_{0.55z}N_{0.45}$ ($0 < y, z < 1$) space. Quasi-ternary phase diagram with the $Li_{1.9}Cl_{0.55}N_{0.45}$, $Li_{1.9}Br_{0.55}N_{0.45}$ and the $Li_{2.45}S_{0.55}N_{0.45}$ compositions at its vertices. The circles represent the phase-compositions that were synthesized as part of this work. Coloured circles signify pure-phase antifluorite-like products. Hollow circles signify no pure-phase antifluorite-like phase product. The colors correspond to experimentally measured ionic conductivities at 22 °C. A schematic unit cell of the phase space investigated is also shown.

288 We find that nearly all compositions in the phase space shown in Figure 6 exist as Li-deficient or Li-excess
289 antifluorite structures. Only highly Br-rich samples where the bromine content exceeds 40% of all anions
290 (that is, values of $z > 0.75$ in $Li_{1.9+0.55y}Cl_{0.55(1-y-z)}S_{0.55y}Br_{0.55z}N_{0.45}$) did not result in phase-pure antifluorite-like
291 phases.

292 Three main trends may be derived from Figure 6. (1) S_{Cl} substitutions entail a continuous increase in ionic
293 conductivity. For instance, when substituting Cl in $Li_{1.9}Cl_{0.55}N_{0.45}$ by S to form $Li_{2.45}S_{0.55}N_{0.45}$ the conductivity
294 increases by an order of magnitude (from 0.02 to 0.15 mS cm⁻¹). This trend can be rationalized based on
295 the increased mobile charge-carrier concentration through charge compensation in replacing S^{2-} by Cl^-
296 ions. (2) The second main trend we derive from Figure 6 is that Br_{Cl} substitutions entail a continuous
297 increase in ionic conductivity. For instance, substituting all Cl in $Li_{2.175}Cl_{0.275}S_{0.275}N_{0.45}$ by Br to from
298 $Li_{2.175}Br_{0.275}S_{0.275}N_{0.45}$ leads to a conductivity increase by a factor of ca. 2. This trend may be rationalized
299 by the larger ion radius of Br^- compared to Cl^- : the presence of Br^- increases the lattice parameter, which
300 facilitates diffusion through the sterically constrained diffusion bottlenecks. Additionally, the higher
301 polarizability (*softness*) of Br compared to Cl (ref ²³) may ease diffusion through Br-containing bottlenecks
302 compared to Cl-containing bottlenecks. (3) The third trend we derive from Figure 6 is that partial Br_S
303 substitutions increase ionic conductivities. Unlike the two previous trends, this trend is not monotonic.
304 While partial Br_S substitution leads to higher conductivities, carrying the substitution too far leads to
305 decreasing conductivities. This discontinuous trend may be explained as follows. While Br_S substitutions
306 increase the lattice parameter, Br_S substitutions concurrently reduce the Li concentration to compensate
307 for the lower valence of Br^- compared to S^{2-} ions.

308 In agreement with the trends described above we find that the phase with the highest conductivity is a
309 moderately Br -substituted $Li_{2.45}S_{0.55}N_{0.45}$ phase – that is a phase with a stoichiometry of $Li_{2.31}S_{0.41}Br_{0.14}N_{0.45}$
310 reaching a conductivity of ca. 0.2 mS cm⁻¹ at 22 °C. Overall this investigation demonstrates the high
311 structural and compositional flexibility of the antifluorite framework; Li-deficient and Li-rich antifluorite
312 phases may be stabilized and may feature numerous elements on the anion site.

313 **Perspectives of irreducible antifluorite-like electrolytes for batteries**

314 Solid-state batteries necessitate high-energy, low-voltage anodes such as Li metal or Li_xSi to supersede
315 conventional Li-ion batteries.^{8,24} However, the best ion conductors known to date —reaching >0.1 mScm⁻¹
316 in conductivity and comprising oxide, sulfide and halide chemistries suffer from electrochemical
317 decomposition <1V vs Li/Li⁺^{7,25–27}— with the exception of garnet oxides which are compatible with Li
318 metal.^{28**} Electrochemical decomposition on the anode side is associated with increased cell resistance,
319 capacity loss, dendrite formation and short-circuiting.^{29,30} A promising strategy to avoid reductive
320 decomposition are bilayer separators comprising a catholyte facing the cathode and an anolyte facing the

** Even oxide garnet electrolytes may potentially benefit from protection layers against Li metal.^{46,47}

321 anode.¹ Anolytes should be highly-conducting and electrochemically stable at the low potentials of Li
322 metal anodes. Highly conducting fully-reduced phases are thus inherently promising anolyte candidates
323 which has also been demonstrated experimentally.^{13,14,31}

324 High conductivity and reductive stability are not the only criteria suitability criteria of anolytes. The
325 suitability of anolyte layers is system-dependent and multiple factors need to be considered. Mechanical
326 and microstructural properties of solid electrolytes play a key role, for instance in dendrite formation and
327 mechanical degradation in solid-state batteries.^{32,33} Chemical compatibilities of anolytes with the paired
328 catholytes also need to be considered.¹⁰ Additionally, the oxidation limit of anolytes needs to be
329 considered; for applications e.g. with Li_xSi anodes whose operation window ranges from 0.01 V to 1.1 V.⁸
330 Due to the low oxidation limit of Li₃N (0.8 V vs Li/Li⁺), Li₃N would be inert to reduction but not inert to
331 oxidation when in contact with Li_xSi anodes. In contrast, some compositions of the antifluorite-like phases
332 have oxidation limits exceeding 1.1 V (see Figure 5c) and would be suitable anolytes for Li_xSi anodes as
333 they would be inert to reduction and oxidation. In summary, irreducible electrolytes are promising anolyte
334 candidates. The high compositional and structural flexibility of fully-reduced antifluorite-like phases we
335 demonstrate in this study will enable the further tunability of ionic conductivity, electrochemical stability,
336 mechanical and microstructural properties – essential for functional electrode/electrolyte interfaces in
337 batteries.³²

338 Conclusion

339 Fully reduced electrolytes based on the antifluorite framework recently received ample attention as their
340 stability against low potentials eliminates performance degradation due to reductive decomposition.³⁴ In
341 this study we demonstrated that the mechanism underlying the increased conductivity in herein
342 discovered irreducible antifluorite-like Li_{1+2x}Cl_{1-x}N_x phases (which includes Li₉N₂Cl₃ ref. ³⁴ and Li₅NCl₂ refs.
343 ^{10,15}) compared to the structurally similar LiCl phase. Computationally, we find that introducing nitrogen
344 into the LiCl anionic framework brings tetrahedral and octahedral Li sites closer in energy so that vacant
345 sites become energetically accessible for diffusion. Analyzing local diffusion bottlenecks we further
346 showed that nitrogen widens diffusion bottlenecks further facilitating Li diffusion. Experimentally we
347 demonstrated that the antifluorite framework is structurally flexible; Li-deficient and Li-excess antifluorite
348 phases can be stabilized. We further found that fully reduced antifluorite-like phases have an increased
349 oxidation limit compared to Li₃N (0.8 V vs Li) which may be critical advantage over Li₃N (the archetypical
350 fully-reduced electrolyte) to stabilize next-generation anodes. Additionally, we showed that Li_{1+2x}Cl_{1-x}N_x
351 phases are compositionally highly modifiable. S_{Cl}⁻ and Br_{Cl}⁻-substituted analogues were synthesized,

352 boosting the ionic conductivities of $\text{Li}_{1+2x}\text{Cl}_{1-x}\text{N}_x$ phases by an order of magnitude. We demonstrate that
353 ternary and quaternary solid solutions can be synthesized mechanochemically in the $\text{LiCl-LiBr-Li}_2\text{S-Li}_3\text{N}$
354 phase space, unlocking an expansive compositional domain for future materials exploration.

355 **Methodology**

356 **Synthesis.** All preparation steps were performed in an argon atmosphere ($\text{H}_2\text{O} < 1 \text{ ppm}$, $\text{O}_2 < 1 \text{ ppm}$).
357 *$\text{Li}_{1+2x}\text{Cl}_{1-x}\text{N}_x$ phases:* The synthesis precursors were LiCl (Sigma-Aldrich, 99%) and Li_3N (Sigma-Aldrich,
358 >99.5%). Stoichiometric amounts of the precursors were milled in a planetary ball mill (Jar: ZrO_2 , 45 mL)
359 with 10 mm ZrO_2 balls and a ball:powder mass ratio of 30 at 550 rpm for 99 (5-min milling-5 min-pause)
360 cycles. *$\text{Li}_{2+x}\text{S}_{1-x}\text{N}_x$ phases* (originally reported in ref. ¹³). The synthesis precursors were Li_2S (Sigma-Aldrich,
361 99%) and Li_3N (Sigma-Aldrich, >99.5%). Stoichiometric amounts of the precursors were milled in a
362 planetary ball mill (Jar: ZrO_2 , 45 mL) with 10 mm ZrO_2 balls and a ball:powder mass ratio of 30 at 550 rpm
363 for 99 (5-min milling-5 min-pause) cycles.

364 **Electrochemical Characterization.** the same procedure was applied to all solid electrolytes (SE)
365 investigated in this work: $\text{Li}_{1+2x}\text{Cl}_{1-x}\text{N}_x$ and $\text{Li}_{2+x}\text{S}_{1-x}\text{N}_x$ and $\text{Li}_{1.9+0.55y}\text{Cl}_{0.55(1-y-z)}\text{S}_{0.55y}\text{Br}_{0.55z}\text{N}_{0.45}$. *Electrochemical*
366 *Impedance Spectroscopy (EIS):* Pellets (diameter=10 mm) of the SE powder samples were pressed (3.2
367 tons) in custom-made cells. These lab cells consist of an alumina tube and two stainless steel (SS) plungers
368 and an airtight seal. The stainless steel plungers act as current collectors. Solid electrolyte powder is filled
369 in the alumina tube and compressed on both sides with the stainless steel plungers. The cell configuration
370 used was SS|SE|SS. AC impedance was performed with a Metrohm Autolab (AUT86298) in the frequency
371 range 10 MHz to 0.1 Hz with a voltage amplitude of 10 mV. EIS spectra were fitted with a resistor in parallel
372 with a constant phase element (CPE) representing the solid electrolyte and a CPE representing the solid
373 electrolyte-SS interface. RT conductivities were measured in ambient conditions (22 °C in our labs). *Linear*
374 *sweep voltammetry (LSV):* LSV measurements were also performed with an Metrohm Autolab
375 (AUT86298). To measure the anodic limit of SE phases, Li|SE|SE-C cells were used. To make the SE-C
376 composite cathode a mixture of SE:Super P with a weight ratio of 0.7:0.3 was milled in a planetary ball
377 mill (Jar: ZrO_2 , 45 mL) with 10 mm ZrO_2 balls and a ball/powder ratio of 30 at 400 rpm for 2 h (5 min
378 milling; 5 min pause). Li| SE | SE -C cells were assembled by pressing a SE pellet (130 mg, 3.2 tons) and
379 subsequently the SE-C composite (15 mg, 3.2 tons) on top. Finally, a Li disk was placed on the opposite
380 side of the SE pellet. The LSV scanning rate was 0.01 mV s⁻¹.

381 **X-ray diffraction.** Powder diffraction patterns were collected using Cu K α X-rays (1.54 Å) on a PANalytical
382 X'Pert Pro X-ray diffractometer. The air sensitive SE probes were loaded into air-tight holders in an Ar-

383 filled glovebox prior to the measurements. GSAS-II³⁵ and FullProf³⁶ used for LeBail and Rietveld
384 refinements. As a starting point the structure solution of Li₅NCl₂ (i.e. Li_{1.66}Cl_{0.66}N_{0.33}) was taken.¹⁵ For
385 Li_{1+2x}Cl_{1-x}N_x phases with higher nitrogen content the nitrogen amount was increased, the chlorine amount
386 reduced and the Li fraction of occupied tetrahedral sites increased according to the synthesized
387 stoichiometry. Based on the initial structure solution of Li_{1.66}Cl_{0.66}N_{0.33} [ref. ¹⁵] all Li ions were assumed in
388 tetrahedral sites though we note that generally a small occupation of the octahedral sites (<=5%) may
389 potentially exist (see Supplementary Note 1).

390 **Computational details.** All DFT calculations were performed with the Vienna ab initio simulation package
391 VASP with computational settings consistent with those used in the Materials Project database.³⁷
392 *Obtaining jump-activation energies for Li_{1+2x}Cl_{1-x}N_x and LiCl.* For the generation and analysis of supercells
393 the calculations were done on 7 different 2x2x2 Li_{1+2x}Cl_{1-x}N_x and one 2x2x2 LiCl supercells. Because of the
394 shared site occupations and partial occupancies in Li_{1+2x}Cl_{1-x}N_x phases, different atomic arrangements were
395 generated by random decoration of the Wyckoff 4a (0,0,0) position with nitrogen and chlorine and the 8c
396 (0.25,0.25,0.25) positions were randomly decorated with Li and vacancies. For the generation and analysis
397 of supercells the pymatgen package was used.³⁸ For the AIMD simulations the Li pseudopotential was
398 changed from one considering the semicore s electrons as valence (i.e. 1s²2s¹ "Li_sv", which was used for
399 relaxations) to one considering the 2s electrons (i.e. 2s¹ "Li") as this enables the use of a lower energy
400 cutoff and vastly improves computational speed. The simulation time was 200 ps for every AIMD
401 simulation. The AIMD simulations were executed at 1000 K. The dissection of AIMD simulations into
402 individual jump events and subsequent analysis of jump frequencies and individual E_{a, jump} values was
403 done as first described by de Klerk and Wagemaker¹⁸ and currently developed as a python package in our
404 group.³⁹ A comprehensive account can be found in ref¹⁸ but crucial aspects for the understanding of the
405 reported data is presented here. *Calculation of E_{a, jump} values between two sites:* The sites are defined
406 around the 0 K equilibrium positions of the Li ions. At every simulation step it is recorded in which site
407 each Li ion is located or whether it is currently between two sites. From this information the jump
408 frequency between two sites v_{A->B} can be calculated according to equation 3:

409

$$v_{A \rightarrow B} = \frac{N_{A \rightarrow B}}{\tau_A} \quad (3)$$

410 where v_{A->B} is the jump frequency for jumps from site A to site B, N_{A->B} is the number of recorded jumps
411 from A to B, and τ_A is the time of occupation of site A. E_{a, jump} is then obtained from equation (1). This
412 analysis can be done with the *gemdat* ref⁽³⁹⁾ python package currently developed in our group. To obtain

413 a picture as complete as possible for the jump processes in the disordered $\text{Li}_{1+2x}\text{Cl}_{1-x}\text{N}_x$ phases we executed
414 the AIMD simulations on 5 supercells that together feature all of the possible site-bottleneck-site
415 permutations in $\text{Li}_{1+2x}\text{Cl}_{1-x}\text{N}_x$ phases. A table with jump E_a values is provided Table S7.

416 *Stability calculations for $\text{Li}_{1+2x}\text{Cl}_{1-x}\text{N}_x$ and for $\text{Li}_{2+x}\text{S}_{1-x}\text{N}_x$.* 10,000 2x2x2 supercells were generated by
417 *randomly decorating* the Wyckoff 4a (0,0,0) position with nitrogen and chlorine. The 8c (0.25,0.25,0.25)
418 positions were also randomly decorated with Li and vacancies according to the targeted stoichiometry.
419 Then formal charges of -3, -1, and +1 were assigned to nitrogen, chlorine and Li, respectively and the
420 electrostatic energy ('Ewald energy') was calculated via *pymatgen*. Subsequently, out of the $\text{Li}_{1+2x}\text{Cl}_{1-x}\text{N}_x$
421 structures, 30 with the lowest Ewald energy were taken and relaxed by DFT. The energies obtained from
422 DFT were used to calculate the energy of the hull of the $\text{Li}_{1+2x}\text{Cl}_{1-x}\text{N}_x$ phases, energetic corrections from the
423 materials project data base were applied and the energies for the end-member phases (Li_3N and Li_2S)
424 were also obtained from the materials project data base (see Supplementary Note 4 also).³⁷

425 Data Availability

426 The data that support the findings of this study and the code to reproduce the results shown in the paper
427 are openly available in 4TU.ResearchData at <https://doi.org/10.4121/fcb46e92-06cd-4241-a97b-3390d6dc1f70>. We used python version 3.10 and the following python packages: numpy [40], gemdat [39],
428 matplotlib [41], pymatgen [38]

430 Author Contributions

431 The study was conceptualized by V.L. Simulation data were acquired by V.L. Experimental data were
432 acquired by V.L, M.T. and Z.C. Data analysis and interpretation were done by V.L., T.F., M.T. and M.W.
433 Writing and editing of the draft were done by V.L., T.F., M.W. The funding for this study was acquired by
434 M.W. and T.F.. The project was supervised by T.F. and M.W. All authors have approved the submitted
435 version of the manuscript.

436 Acknowledgements

437 M.W. and V.L. acknowledge the funding received from the Netherlands Organization for Scientific
438 Research (NWO) under the VICI grant (no. 16122). T.F. acknowledges the funding provided by the
439 European Union's HORIZON EUROPE programme in the form of a Marie Skłodowska-Curie individual
440 postdoctoral fellowship (project no. 101066486). A.V. acknowledges financial support from the
441 Netherlands Organization for Scientific Research (NWO) under the VENI grant number 18123 and the
442 eScience Centre under the NLESC.OEC.2022.013. grant. T.F., A.V. and V.L. acknowledge financial support

443 by the NWO in the form of an open-competition XS grant (OCENW.XS22.4.210). All authors acknowledge
444 the use of computational resources of the DelftBlue supercomputer, provided by Delft High Performance
445 Computing Centre (<https://www.tudelft.nl/dhpc>).

446 **References**

447 The following references used in the Supplementary Information: ^{13,15,37,42,43}

- 448 (1) Famprakis, T.; Canepa, P.; Dawson, J. A.; Islam, M. S.; Masquelier, C. Fundamentals of
449 Inorganic Solid-State Electrolytes for Batteries. *Nat. Mater.* **2019**.
- 450 (2) Janek, J.; Zeier, W. G. Challenges in Speeding up Solid-State Battery Development. *Nat.*
451 *Energy* **2023**, *8* (3), 230–240.
- 452 (3) Kato, Y.; Hori, S.; Saito, T.; Suzuki, K.; Hirayama, M.; Mitsui, A.; Yonemura, M.; Iba, H.;
453 Kanno, R. High-Power All-Solid-State Batteries Using Sulfide Superionic Conductors. *Nat.*
454 *Energy* **2016**, *1* (March), 16030.
- 455 (4) Zhou, L.; Assoud, A.; Zhang, Q.; Wu, X.; Nazar, L. F. New Family of Argyrodite
456 Thioantimonate Lithium Superionic Conductors. *J. Am. Chem. Soc.* **2019**, *141* (48), 19002–
457 19013.
- 458 (5) Kraft, M. A.; Ohno, S.; Zinkevich, T.; Koerver, R.; Culver, S. P.; Fuchs, T.; Senyshyn, A.; Indris,
459 S.; Morgan, B. J.; Zeier, W. G. Inducing High Ionic Conductivity in the Lithium Superionic
460 Argyrodites $\text{Li}_{6+x}\text{P}_{1-x}\text{Ge}_x\text{S}_5\text{I}$ for All-Solid-State Batteries. *J. Am. Chem. Soc.* **2018**, *140*
461 (47), 16330–16339.
- 462 (6) Kamaya, N.; Homma, K.; Yamakawa, Y.; Hirayama, M.; Kanno, R.; Yonemura, M.;
463 Kamiyama, T.; Kato, Y.; Hama, S.; Kawamoto, K.; Mitsui, A. A Lithium Superionic Conductor.
464 *Nat. Mater.* **2011**, *10* (9), 682–686.
- 465 (7) Zhu, Y.; He, X.; Mo, Y. First Principles Study on Electrochemical and Chemical Stability of
466 Solid Electrolyte-Electrode Interfaces in All-Solid-State Li-Ion Batteries. *J. Mater. Chem. A*
467 **2016**, *4* (9), 3253–3266.
- 468 (8) Huo, H.; Janek, J. Silicon as Emerging Anode in Solid-State Batteries. *ACS Energy Lett.* **2022**,

- 469 7 (11), 4005–4016.
- 470 (9) Zaman, W.; Hatzell, K. B. Processing and Manufacturing of next Generation Lithium-Based
471 All Solid-State Batteries. *Curr. Opin. Solid State Mater. Sci.* **2022**, *26* (4), 101003.
- 472 (10) Landgraf, V.; Famprakis, T.; de Leeuw, J.; Bannenberg, L. J.; Ganapathy, S.; Wagemaker, M.
473 Li₅NCl₂: A Fully-Reduced, Highly-Disordered Nitride-Halide Electrolyte for Solid-State
474 Batteries with Lithium-Metal Anodes. *ACS Appl. Energy Mater.* **2023**, *6* (3), 1661–1672.
- 475 (11) Szczuka, C.; Karasulu, B.; Groh, M. F.; Sayed, F. N.; Sherman, T. J.; Bocarsly, J. D.; Vema, S.;
476 Menkin, S.; Emge, S. P.; Morris, A. J.; Grey, C. P. Forced Disorder in the Solid Solution Li₃P–
477 Li₂S: A New Class of Fully Reduced Solid Electrolytes for Lithium Metal Anodes. *J. Am.*
478 *Chem. Soc.* **2022**, *144* (36), 16350–16365.
- 479 (12) Xu, X.; Du, G.; Cui, C.; Liang, J.; Zeng, C.; Wang, S.; Ma, Y.; Li, H. Stabilizing the Halide Solid
480 Electrolyte to Lithium by a β-Li₃N Interfacial Layer. *ACS Appl. Mater. Interfaces* **2022**, *14*
481 (35), 39951–39958.
- 482 (13) Landgraf, V.; Tu, M.; Cheng, Z.; de Leeuw, J.; Ganapathy, S.; Wagemaker, M.; Famprakis, T.
483 Entropy-Induced High Conductivity in Fully-Reduced Electrolytes for Solid-State Batteries
484 with Lithium Metal Anodes. *ChemRxiv*. November 7, 2023.
- 485 (14) Li, W.; Li, M.; Chien, P.-H.; Wang, S.; Yu, C.; King, G.; Hu, Y.; Xiao, Q.; Shakouri, M.; Feng, R.
486 Lithium-Compatible and Air-Stable Vacancy-Rich Li₉N₂Cl₃ for High–Areal Capacity, Long-
487 Cycling All–Solid-State Lithium Metal Batteries. *Sci. Adv.* **2023**, *9* (42), eadh4626.
- 488 (15) Marx, R.; Mayer, H. M. Preparation and Crystal Structure of Ordered and Disordered
489 Lithium Nitride Dichloride, Li₅NCl₂. *J. Solid State Chem.* **1997**, *130* (1), 90–96.
- 490 (16) Weppner, W.; Hartwig, P.; Rabenau, A. Consideration of Lithium Nitride Halides as Solid
491 Electrolytes in Practical Galvanic Cell Applications. *J. Power Sources* **1981**, *6* (3), 251–259.
- 492 (17) Shannon, R. D. Revised Effective Ionic Radii and Systematic Studies of Interatomic
493 Distances in Halides and Chalcogenides. *Acta Crystallogr. Sect. A Cryst. physics, diffraction,*
494 *Theor. Gen. Crystallogr.* **1976**, *32* (5), 751–767.

- 495 (18) De Klerk, N. J. J.; Van Der Maas, E.; Wagemaker, M. Analysis of Diffusion in Solid-State
496 Electrolytes through MD Simulations, Improvement of the Li-Ion Conductivity in β -Li₃PS₄
497 as an Example. *ACS Appl. Energy Mater.* **2018**, *1* (7), 3230–3242.
- 498 (19) Yu, C.; Ganapathy, S.; De Klerk, N. J. J.; Roslon, I.; Van Eck, E. R. H.; Kentgens, A. P. M.;
499 Wagemaker, M. Unravelling Li-Ion Transport from Picoseconds to Seconds: Bulk versus
500 Interfaces in an Argyrodite Li₆PS₅Cl-Li₂S All-Solid-State Li-Ion Battery. *J. Am. Chem. Soc.*
501 **2016**, *138* (35), 11192–11201.
- 502 (20) De Klerk, N. J. J.; Rostón, I.; Wagemaker, M. Diffusion Mechanism of Li Argyrodite Solid
503 Electrolytes for Li-Ion Batteries and Prediction of Optimized Halogen Doping: The Effect of
504 Li Vacancies, Halogens, and Halogen Disorder. *Chem. Mater.* **2016**, *28* (21), 7955–7963.
- 505 (21) De Klerk, N. J. J.; Wagemaker, M. Diffusion Mechanism of the Sodium-Ion Solid Electrolyte
506 Na₃PS₄ and Potential Improvements of Halogen Doping. *Chem. Mater.* **2016**, *28* (9), 3122–
507 3130.
- 508 (22) Li, X.; Liu, H.; Zhao, C.; Kim, J. T.; Fu, J.; Hao, X.; Li, W.; Li, R.; Chen, N.; Cao, D.; Wu, Z.; Su,
509 Y.; Liang, J.; Sun, X. Hopping Rate and Migration Entropy as the Origin of Superionic
510 Conduction within Solid-State Electrolytes. *J. Am. Chem. Soc.* **2023**, *145* (21), 11701–
511 11709.
- 512 (23) Flores-González, N.; Minafra, N.; Dewald, G.; Reardon, H.; Smith, R. I.; Adams, S.; Zeier, W.
513 G.; Gregory, D. H. Mechanochemical Synthesis and Structure of Lithium
514 Tetrahaloaluminates, LiAlX₄(X = Cl, Br, I): A Family of Li-Ion Conducting Ternary Halides.
515 *ACS Mater. Lett.* **2021**, *3* (5), 652–657.
- 516 (24) Janek, J.; Zeier, W. G. A Solid Future for Battery Development. *Nat. Energy* **2016**, *1* (9), 1–
517 4.
- 518 (25) Zhu, Y.; He, X.; Mo, Y. Origin of Outstanding Stability in the Lithium Solid Electrolyte
519 Materials: Insights from Thermodynamic Analyses Based on First-Principles Calculations.
520 *ACS Appl. Mater. Interfaces* **2015**, *7* (42), 23685–23693.

- 521 (26) Schwietert, T. K.; Arszelewska, V. A.; Wang, C.; Yu, C.; Vasileiadis, A.; de Clerk, N. J. J.;
522 Hageman, J.; Hupfer, T.; Kerkamm, I.; Xu, Y. Clarifying the Relationship between Redox
523 Activity and Electrochemical Stability in Solid Electrolytes. *Nat. Mater.* **2020**, *19* (4), 428–
524 435.
- 525 (27) Wang, S.; Bai, Q.; Nolan, A. M.; Liu, Y.; Gong, S.; Sun, Q.; Mo, Y. Lithium Chlorides and
526 Bromides as Promising Solid-State Chemistries for Fast Ion Conductors with Good
527 Electrochemical Stability. *Angew. Chemie - Int. Ed.* **2019**, *58* (24), 8039–8043.
- 528 (28) Subramanian, K.; Alexander, G. V; Karthik, K.; Patra, S.; Indu, M. S.; Sreejith, O. V;
529 Viswanathan, R.; Narayanasamy, J.; Murugan, R. A Brief Review of Recent Advances in
530 Garnet Structured Solid Electrolyte Based Lithium Metal Batteries. *J. Energy Storage* **2021**,
531 33, 102157.
- 532 (29) Riegger, L. M.; Schlem, R.; Sann, J.; Zeier, W. G.; Janek, J. Lithium-Metal Anode Instability
533 of the Superionic Halide Solid Electrolytes and the Implications for Solid-State Batteries.
534 *Angew. Chemie* **2021**, *133* (12), 6792–6797.
- 535 (30) Du, M.; Liao, K.; Lu, Q.; Shao, Z. Recent Advances in the Interface Engineering of Solid-State
536 Li-Ion Batteries with Artificial Buffer Layers: Challenges, Materials, Construction, and
537 Characterization. *Energy Environ. Sci.* **2019**, *12* (6), 1780–1804.
- 538 (31) Yu, P.; Zhang, H.; Hussain, F.; Luo, J.; Tang, W.; Lei, J.; Gao, L.; Butenko, D.; Wang, C.; Zhu,
539 J.; Yin, W.; Zhang, H.; Han, S.; Zou, R.; Chen, W.; Zhao, Y.; Xia, W.; Sun, X. Lithium Metal-
540 Compatible Antifluorite Electrolytes for Solid-State Batteries. *J. Am. Chem. Soc.* **2024**.
- 541 (32) Krauskopf, T.; Richter, F. H.; Zeier, W. G.; Janek, J. Physicochemical Concepts of the Lithium
542 Metal Anode in Solid-State Batteries. *Chem. Rev.* **2020**, *120* (15), 7745–7794.
- 543 (33) Hatzell, K. B.; Chen, X. C.; Cobb, C. L.; Dasgupta, N. P.; Dixit, M. B.; Marbella, L. E.; McDowell,
544 M. T.; Mukherjee, P. P.; Verma, A.; Viswanathan, V.; Westover, A. S.; Zeier, W. G.
545 Challenges in Lithium Metal Anodes for Solid- State Batteries. **2020**.
- 546 (34) Li, W.; Li, M.; Chien, P.; Wang, S.; Yu, C.; King, G.; Hu, Y.; Xiao, Q.; Shakouri, M.; Feng, R.;

- 547 Fu, B.; Abdolvand, H.; Fraser, A.; Li, R.; Huang, Y.; Liu, J.; Mo, Y.; Sham, T.; Sun, X. Lithium-
548 Compatible and Air-Stable Vacancy-Rich $\text{Li}_9\text{N}_2\text{Cl}_3$ for High – Areal Capacity , Long-Cycling
549 All – Solid-State Lithium Metal Batteries. **2023**.
- 550 (35) Toby, B. H.; Von Dreele, R. B. GSAS-II: The Genesis of a Modern Open-Source All Purpose
551 Crystallography Software Package. *J. Appl. Crystallogr.* **2013**, *46* (2), 544–549.
- 552 (36) Rodriguez-Carvajal, J. In Satellite Meeting on Powder Diffraction of the XV Congress of the
553 IUCr, 1990, 127. *Toulouse, Fr.*
- 554 (37) Jain, A.; Ong, S. P.; Hautier, G.; Chen, W.; Richards, W. D.; Dacek, S.; Cholia, S.; Gunter, D.;
555 Skinner, D.; Ceder, G.; Persson, K. A. Commentary: The Materials Project: A Materials
556 Genome Approach to Accelerating Materials Innovation. *APL Mater.* **2013**, *1* (1), 001002.
- 557 (38) Ong, S. P.; Richards, W. D.; Jain, A.; Hautier, G.; Kocher, M.; Cholia, S.; Gunter, D.; Chevrier,
558 V. L.; Persson, K. A.; Ceder, G. Python Materials Genomics (Pymatgen): A Robust, Open-
559 Source Python Library for Materials Analysis. *Comput. Mater. Sci.* **2013**, *68*, 314–319.
- 560 (39) Azizi, V.; Smeets, S.; Lavrinenko, A. K.; Ciarella, S.; Famprakis, T. GEMDAT. Zenodo July 2024.
- 561 (40) Harris, C. R.; Millman, K. J.; Van Der Walt, S. J.; Gommers, R.; Virtanen, P.; Cournapeau, D.;
562 Wieser, E.; Taylor, J.; Berg, S.; Smith, N. J. Array Programming with NumPy. *Nature* **2020**,
563 *585* (7825), 357–362.
- 564 (41) Hunter, J. D. Matplotlib: A 2D Graphics Environment. *Comput. Sci. \& Eng.* **2007**, *9* (3), 90–
565 95.
- 566 (42) Catlow, C. R. A. STATIC LATTICE SIMULATION OF STRUCTURE AND TRANSPORT IN
567 SUPERIONIC CONDUCTORS. *Solid State Ionics* **1983**, *8* (SUPPL. 3), 89–107.
- 568 (43) Marx, R.; Lissner, F.; Schleid, T. $\text{Li}_9\text{N}_2\text{S}_3$: Das Erste Nitridsulfid Der Alkalimetalle in Einer
569 Li_2O -Typ-Variante. *Zeitschrift für Anorg. und Allg. Chemie* **2006**, *632* (12-13), 2151.
- 570 (44) Deng, Z.; Mishra, T. P.; Mahayoni, E.; Ma, Q.; Tieu, A. J. K.; Guillon, O.; Chotard, J.-N.;
571 Seznec, V.; Cheetham, A. K.; Masquelier, C. Fundamental Investigations on the Sodium-Ion
572 Transport Properties of Mixed Polyanion Solid-State Battery Electrolytes. *Nat. Commun.*

- 573 **2022**, **13** (1), 4470.
- 574 (45) Wilkening, M.; Gebauer, D.; Heitjans, P. Diffusion Parameters in Single-Crystalline Li₃N as
575 Probed by ⁶Li and ⁷Li Spin-Alignment Echo NMR Spectroscopy in Comparison with Results
576 from ⁸Li β-Radiation Detected NMR. *J. Phys. Condens. Matter* **2007**, **20** (2), 22201.
- 577 (46) Xu, H.; Li, Y.; Zhou, A.; Wu, N.; Xin, S.; Li, Z.; Goodenough, J. B. Li₃N-Modified Garnet
578 Electrolyte for All-Solid-State Lithium Metal Batteries Operated at 40 °c. *Nano Lett.* **2018**,
579 18 (11), 7414–7418.
- 580 (47) Zhu, C.; Fuchs, T.; Weber, S. A. L.; Richter, F. H.; Glasser, G.; Weber, F.; Butt, H. J.; Janek, J.;
581 Berger, R. Understanding the Evolution of Lithium Dendrites at Li_{6.25}Al_{0.25}La₃Zr₂O₁₂ Grain
582 Boundaries via Operando Microscopy Techniques. *Nat. Commun.* **2023**, **14** (1), 1300.
- 583
- 584